Rotation Estimation based on Anisotropic Angular Radon Spectrum

Dario Lodi Rizzini[1,2] and Ernesto Fontana[1]

Abstract—In this paper, we present the anisotropic Angular Radon Spectrum (ARS), a novel feature for global estimation of rotation in a two dimension space. ARS effectively describes collinearity of points and has the properties of translation-invariance and shift-rotation. We derive the analytical expression of ARS for Gaussian Mixture Models (GMM) representing point clouds where the Gaussian kernels have arbitrary covariances. Furthermore, we developed a preliminary procedure for simplification of GMM suitable for efficient computation of ARS. Rotation between point clouds is estimated by searching of maximum of correlation between their spectra. Correlation is efficiently computed from Fourier series expansion of ARS. Experiments on datasets of distorted object shapes, laser scans and on robotic mapping datasets assess the accuracy and robustness to noise in global rotation estimation.

Index Terms—Mapping; Rotation estimation

I. INTRODUCTION

THE alignment of point clouds is an important primitive for many applications in robot localization and mapping. This operation is also known as registration and allows merging of views of the same object or scene differing in orientation and position. The standard approach to registration requires detection of corresponding parts between the two views, which are usually represented in the form of point clouds. Correspondence-based methods [1]–[5] estimate the rigid transformation by minimizing the distances between corresponding points in the two compared point sets. The computation of rigid transformation has well known closed-form solution for 2D, 3D and arbitrary dimensions, but in order to establish correct point-to-point or point-to-surface associations a good initial guess of the transformation is required. Inaccurate correspondences often lead to wrong estimation, since standard registration methods only solve local optimization problems.

Unfortunately, the availability of initial guess is retrieved by another measurement (e.g. the robot odometry) or by preliminary feature matching [3]. Robust associations techniques like Vector Field Consensus (VFC) [2] and Procrustes analysis for deformable objects [5] have been proposed to detect consistent associations and filter outliers associations. Formally guaranteed methods like TEASER [4] effectively estimate with high number of outlier associations, but they may still fail with highly inaccurate initial correspondences. They exploit regularization and other consensus techniques to remove outlier associations. Global registration methods [6], [7] provide guaranteed global optimal solution with branch-and-bound search, but are not adequately efficient for practical applications. Another category of global methods model the input point clouds as a continuous functions like a Bayesian model of normals [8] or kernel Hilbert space [9], [10] and perform global optimization.

Global registration algorithms often rely on features like local descriptors, global histograms or functions extracted from each point set. Several correspondence-less methods enable separation between estimation of rotation and of translation. They include PCA-based techniques [5], Hough Spectrum (HS) [11], [12] and Angular Radon Spectrum (ARS) [13], Fourier and spherical harmonics expansion of point distributions [14], [15]. A classic approach to registration in 2D domain uses correlation of occupancy grid map [16], which is effective once the discretization parameters have been properly tuned. This approach estimates the transformation between point clouds though global optimization of objectives functions depending on the features. Then, the feature viewpoint invariance is a major factor. Several algorithms allow decoupling of rotation and translation estimation thanks to independence of the features.

In this paper, we propose the planar *anisotropic Angular Radon Spectrum* (ARS), a novel global feature associated to point clouds that enables globally optimal estimation of rotation. ARS effectively describes collinearity relations among the 2D points of a set, possibly the simplest and strongest property that is invariant to rigid motion. It is related to HS [11], a histogram weighting point collinearity to angular directions which is derived from Hough Transform. However, ARS has the form of continuous function computed from a Gaussian mixture model (GMM) representing the distribution of a set of noisy points. It provides a sound mathematical measure of the point density along each pencil of lines. Contrary to HS, it is exactly invariant to translation and a rotation induces an angle-shift without affecting the function shape. In our previous work [13], we formulated ARS for GMMs with isotropic and identical Gaussian kernels, proposed a convenient Fourier series expansion and a correlation function serving as objective function for global optimization of rotation estimation. A Gaussian distribution is isotropic
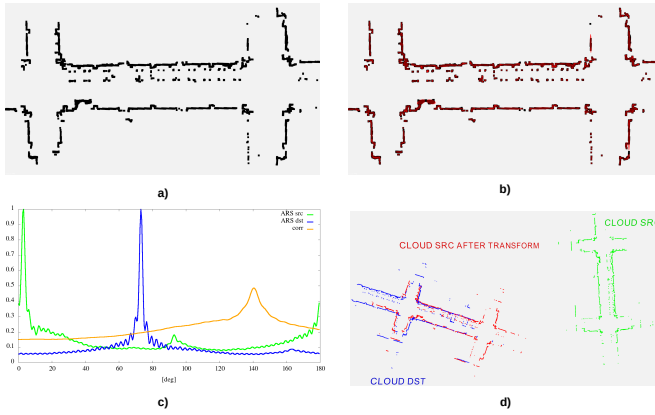
Fig. 1: Visual steps of rotation estimation through Anisotropic ARS: a) point cloud representing planar mapping data; b) simplification of initial point set kernel representation through GMM; c) spectra of ARS on source and destination clouds, and correlation between the two; d) result of consecutive maps alignment through Anisotropic ARS.

if its covariance matrix has the same eigenvalues and the distribution is identical from all the directions. In general, the distribution of noisy point sets is more correctly and efficiently represented by general anisotropic Gaussian kernels. Unfortunately, the analytical expression of ARS function is not as straightforward as in the case of isotropic kernels. The original contributions of this paper are the following.

1) We derive the general expression of ARS for the case of anisotropic GMMs representing the distribution of 2D point sets.
2) We present an effective and novel procedure for GMM simplification as well as the numerical computation of the approximated Fourier series expansion of the anisotropic ARS, the spectrum correlation and its application to rotation estimation.

We also present a procedure for computation of general GMMs from input point clouds and for translation estimation. Experiments illustrate the accuracy and robustness of rotation estimation with the proposed anisotropic ARS compared to local and global state-of-the-art algorithms.

This paper is organized as follows. Section II presents the problem definition and the Radon transform of a GMM. Section III illustrates the expression of anisotropic ARS. Section IV shows how to compute the rotation through correlation of a pair of ARSs. Section V shows experimental results on standard datasets. Finally, Section VI gives the concluding remarks.

II. RADON TRANSFORM OF A GAUSSIAN MIXTURE MODEL

Let $\mathcal{P} = \{\boldsymbol{\mu}_i\}_{i=1,\ldots,n_p}$ with $\boldsymbol{\mu}_i \in \mathbb{R}^2$ be the estimated position vectors of the points. It is convenient to define the *density function* $f : \mathbb{R}^2 \to \mathbb{R}_{\geqslant 0}$ that represents the point density in the plane and is proportional to the probability density function (PDF) of finding a point. If the point positions are exactly known, then the density function consists of Dirac impulse distributions, i.e. $f(\mathbf{r}) = \sum_{i=1}^{n_p}(1/n_p)\delta(\mathbf{r} - \boldsymbol{\mu}_i)$.

However, in most problems the point coordinates are estimated with a given uncertainty and the function $f(\mathbf{r})$ should represent a looser concentration around the input points. The GMM [8], [13] is a widely used model in kernel density estimation and other machine learning applications. According to this model, each point is associated to a Gaussian kernel $\mathcal{N}(\boldsymbol{\mu}_i, \boldsymbol{\Sigma}_i)$ centered on $\boldsymbol{\mu}_i$ and with covariance matrix $\boldsymbol{\Sigma}_i$. The following symbols are used for respectively Mahalanobis distance and Gaussian PDF function

$$\|\mathbf{v}\|_{\Sigma}^2 = \mathbf{v}^\top \boldsymbol{\Sigma}^{-1}\mathbf{v} \tag{1}$$

$$\mathrm{n}\left(\mathbf{v}, \boldsymbol{\Sigma}\right) = (2\pi|\boldsymbol{\Sigma}|)^{-dim(\mathbf{v})/2}\ \exp\left(-\|\mathbf{v}\|_{\boldsymbol{\Sigma}}^2/2\right) \tag{2}$$

Thus, a set of points modeled with GMM has the probability density function

$$f(\mathbf{r}) = \sum_{i=1}^{n_p} w_i\ f_i(\mathbf{r}) = \sum_{i=1}^{n_p} w_i\ \mathrm{n}\left(\mathbf{r} - \boldsymbol{\mu}_i, \boldsymbol{\Sigma}_i\right) \tag{3}$$

where the positive weights $w_i \geqslant 0$ are such that their sum is equal to 1. Given a point distribution model, the goal is to measure the alignment of the point set to a line. Such measure is provided by the *Radon Transform* (RT) [17]. In the most general case, the RT is a functional that associates a function $f(\cdot)$ with values in $\mathbb{R}^d$ to its integral over a $d-1$ dimension manifold $\mathcal{F}_\mathbf{q} \subset \mathbb{R}^d$ with parameter $\mathbf{q}$.

$$\mathcal{R}[f](\mathbf{q}) = \int_{\mathcal{F}_\mathbf{q}} f(\mathbf{r})\ d\mathbf{r} = \sum_{i=1}^{n_p} w_i \int_{\mathcal{F}_\mathbf{q}} \mathrm{n}\left(\mathbf{r} - \boldsymbol{\mu}_i, \boldsymbol{\Sigma}_i\right)\ d\mathbf{r} \tag{4}$$

In our case, $\mathcal{F}_\mathbf{q}$ is a line represented by its polar parameters $\mathbf{q} = [\theta, \rho]^\top$ and the equation of a point in $\mathcal{F}_\mathbf{q}$ is

$$\mathbf{r}(\mathbf{t}) = t_1\ \mathbf{u}_1 + t_2\ \mathbf{u}_2 = \mathbf{U}\mathbf{t} \tag{5}$$

where $t_1 = \rho$ is a fixed constant, t_2 is the parameter associated to the points on the line, $\mathbf{u}_1 = \hat{\mathbf{u}}(\theta) = [\cos\theta, \sin\theta]^\top$ is the unitary vector orthogonal to the line and $\mathbf{u}_2 = \hat{\mathbf{u}}(\theta + \pi/2) = [-\sin\theta, \cos\theta]^\top$ corresponds to the line direction. The matrix $\mathbf{U} = [\mathbf{u}_1, \mathbf{u}_2]$ is an orthonormal matrix. The Radon transform in eq. (4) becomes the integral of $f(\mathbf{U}\mathbf{t})$ in the parameter t_2.

Let us focus on each single Gaussian kernel $f_i(\mathbf{r})$. Since $\mathbf{r} \sim \mathcal{N}(\boldsymbol{\mu}_i, \boldsymbol{\Sigma}_i)$ and $\mathbf{t}$ is a linear transformation of $\mathbf{r}$, i.e. $\mathbf{t} = \mathbf{U}^\top\mathbf{r}$, $\mathbf{t}$ is also Gaussian [18] and, in particular, $\mathbf{t} \sim \mathcal{N}(\tilde{\boldsymbol{\mu}}_i, \tilde{\boldsymbol{\Sigma}}_i)$

$$f_i(\mathbf{r}) = \mathrm{n}\left(\mathbf{r} - \boldsymbol{\mu}_i, \boldsymbol{\Sigma}_i\right) = \mathrm{n}\left(\mathbf{t} - \tilde{\boldsymbol{\mu}}_i, \tilde{\boldsymbol{\Sigma}}_i\right) = f_i(\mathbf{t}) \tag{6}$$

where $\tilde{\boldsymbol{\mu}}_i = \mathbf{U}^\top \boldsymbol{\mu}_i$ and $\tilde{\boldsymbol{\Sigma}}_i = \mathbf{U}^\top \boldsymbol{\Sigma}_i \mathbf{U}$. After the variable change, the computation of Radon Transform of eq. (6) is straightforward, since the integral of the Gaussian Kernel function in t_2 is equivalent to the marginalization of the distribution. The marginal distribution $t_1 \sim \mathcal{N}(\tilde{\mu}_{i,1}, \tilde{\sigma}_{i,1}^2)$ has mean value and covariance equal to

$$\tilde{\mu}_{i,1} = \mathbf{u}_1^\top \boldsymbol{\mu}_i \quad\quad \tilde{\sigma}_{i,1}^2 = \mathbf{u}_1^\top \boldsymbol{\Sigma}_i \mathbf{u}_1 \tag{7}$$

Thus, the RT of a single Gaussian kernel has the form of a Gaussian function as

$$\mathcal{R}[f_i](\theta, \rho) = \mathrm{n}\left(\rho - \tilde{\mu}_{i,1}, \tilde{\sigma}_{i,1}^2\right) \tag{8}$$

where we substituted $t_1 = \rho$ and the values of mean $\tilde{\mu}_{i,1}$ an variance $\tilde{\sigma}_{i,1}^2$ depend on the angle θ of $\mathbf{U}$. The covariance

matrix is decomposed into the product $\mathbf{\Sigma}_i = \mathbf{R}(\gamma_i)\mathbf{\Lambda}_i\mathbf{R}^\top(\gamma_i)$, where $\mathbf{R}(\gamma_i)$ is a rotation matrix by angle γ_i and the diagonal matrix $\mathbf{\Lambda}_i = diag([\overline{\sigma}_i^2, \underline{\sigma}_i^2])$ where the $0 \leqslant \underline{\sigma}_i^2 \leqslant \overline{\sigma}_i^2$ are the eigenvalues of $\mathbf{\Sigma}_i$. Thus, the variance $\tilde{\sigma}_{i,1}^2$ of the marginal can be rewritten as

$$\tilde{\sigma}_{i,1}^2(\theta) = \hat{\mathbf{u}}^\top(\theta)\ \mathbf{R}^\top(\gamma_i)\ \mathbf{\Lambda}_i\ \mathbf{R}(\gamma_i)\ \hat{\mathbf{u}}(\theta) \qquad (9)$$

$$= \hat{\sigma}_i^2\ (1 + \delta_i\ \cos(2\theta - 2\gamma_i)) \qquad (10)$$

where we have substituted $\hat{\sigma}_i^2 = (\overline{\sigma}_i^2 + \underline{\sigma}_i^2)/2$ and $\delta_i = (\overline{\sigma}_i^2 - \underline{\sigma}_i^2)/(\overline{\sigma}_i^2 + \underline{\sigma}_i^2)$. Observe that

$$0 \leqslant \hat{\sigma}_i^2(1 - \delta_i) \leqslant \tilde{\sigma}_{i,1}^2(\theta) \leqslant \hat{\sigma}_i^2(1 + \delta_i) \qquad (11)$$

and, in the case of isotropic covariance, $\delta_i = 0$ and $\tilde{\sigma}_{i,1}^2(\theta)$ is constant.

III. ANGULAR RADON SPECTRUM

Radon Spectra are functionals applied to the Radon Transform in order to detect specific patterns with respect to one of the line parameters. Geometrically, Radon Transform measures the concentration of point distribution on a line defined by parameters $\mathbf{q} = [\theta, \rho]^\top$. If θ is fixed and ρ is free to assume arbitrary values, then the equation represents a family of parallel lines. Radon Spectrum operates on Radon Transform in order to highlight concentration patterns over each family of lines identified by a given direction θ. Such concentration patterns enable characterization of orientation and, thus, can be exploited to perform registration between two point sets. The *Angular Radon Spectrum* (ARS) is defined as

$$\mathcal{S}\left[f\right](\theta) = \int_{-\infty}^{+\infty} \kappa\left(\mathcal{R}[f](\theta, \rho)\right)\ d\rho \qquad (12)$$

where the function $\kappa(\cdot)$ is called *concentration function*. The concentration function $\kappa : \mathbb{R}_{\geqslant 0} \to \mathbb{R}_{\geqslant 0}$ must be strictly super-additive, i.e. $\kappa(x + y) > \kappa(x) + \kappa(y)$ for $0 < x \leqslant y$. If only simple superadditivity holds, i.e. $\kappa(x + y) \geqslant \kappa(x) + \kappa(y)$, the resulting spectra may not properly discriminate the parameters with maxima. Following the suggestion in [11], the function $\kappa(x) = x^2$ is implicitly used in the remaining. Thus, the square of a sum of Gaussian kernels $\kappa(\mathcal{R}[f])$ in eq. (3) consists of double products of Gaussians

$$\kappa\left(\mathcal{R}[f]\right) = \sum_{i=1}^{n_p}\sum_{j=1}^{n_p} w_i\ w_j\ \pi_{ij}(\rho, \theta) \qquad (13)$$

where the double product π_{ij} can be rewritten using the formula about the product of Gaussian densities [19, sec. 8.1.8, p. 42] as

$$\pi_{ij}(\rho, \theta) = \mathrm{n}\left(\rho - \tilde{\mu}_{i,1}, \tilde{\sigma}_{i,1}^2\right)\mathrm{n}\left(\rho - \tilde{\mu}_{j,1}, \tilde{\sigma}_{j,1}^2\right)$$

$$= \mathrm{n}\left(\tilde{\mu}_{j,1} - \tilde{\mu}_{i,1}, \tilde{\sigma}_{j,1}^2 + \tilde{\sigma}_{i,1}^2\right)\mathrm{n}\left(\rho - \tilde{\mu}_{ij}, \tilde{\sigma}_{ij}^2\right) \quad (14)$$

where $\tilde{\mu}_{ij} = \tilde{\sigma}_{ij}^2(\tilde{\sigma}_{i,1}^{-2}\tilde{\mu}_{i,1} + \tilde{\sigma}_{j,1}^{-2}\tilde{\mu}_{j,1})$ and $\tilde{\sigma}_{ij}^2 = (\tilde{\sigma}_{i,1}^{-2} + \tilde{\sigma}_{j,1}^{-2})^{-1}$. The integral of each double product in ρ has a simple expression due to the normalization of Gaussian function

$$\psi_{ij}(\theta) = \int_{-\infty}^{+\infty} \pi_{ij}(\rho, \theta)d\rho = \mathrm{n}\left(\tilde{\mu}_{i,1} - \tilde{\mu}_{j,1}, \tilde{\sigma}_{i,1}^2 + \tilde{\sigma}_{j,1}^2\right)$$

$$= \frac{1}{\sqrt{2\pi\ b_{ij}(\theta)}}\ e^{-\frac{a_{ij}(\theta)}{2\ b_{ij}(\theta)}} \qquad (15)$$

The terms $a_{ij}(\theta)$ and $b_{ij}(\theta)$ of the kernel function are

$$a_{ij}(\theta) = (\mathbf{u}_1^\top(\boldsymbol{\mu}_i - \boldsymbol{\mu}_j))^2 = \frac{m_{ij}^2}{2}\left(1 + \cos(2\theta - 2\beta_{ij})\right) \qquad (16)$$

$$b_{ij}(\theta) = \mathbf{u}_1^\top(\mathbf{\Sigma}_i + \mathbf{\Sigma}_j)\mathbf{u}_1 = \hat{\sigma}_{ij}^2\left(1 + \delta_{ij}\cos(2\theta - 2\gamma_{ij})\right) \qquad (17)$$

where parameters (m_{ij}, β_{ij}) are such that $\boldsymbol{\mu}_j - \boldsymbol{\mu}_i = m_{ij}\mathbf{u}(\beta_{ij})$ and $(\hat{\sigma}_{ij}^2, \gamma_{ij}, \delta_{ij})$ are defined according to eq. (10) referred to matrix $\mathbf{\Sigma}_i + \mathbf{\Sigma}_j$.

Thus, the ARS of a GMM has the form of a summation of kernels $\psi_{ij}(\theta)$ defined for each pair of Gaussians i, j

$$\mathcal{S}\left[f\right](\theta) = \sum_{i=1}^{n_p}\sum_{j=1}^{n_p} w_i\ w_j\ \psi_{ij}(\theta) \qquad (18)$$

The general ARS satisfies the following important property.

Proposition 1 (Translation-invariance and Rotation-shift). *Let $f(\mathbf{r})$ be a GMM subject to rotation $\mathbf{R}(\delta) = \mathbf{R} \in SO(2)$ and translation $\mathbf{t} \in \mathbb{R}^2$. Then, its ARS is equal to*

$$\mathcal{S}\left[f(\mathbf{R}(\delta)\ \mathbf{r} + \mathbf{t})\right](\theta) = \mathcal{S}\left[f(\mathbf{r})\right](\theta + \delta) \qquad (19)$$

where the transformed spectrum does not depend on translation vector $\mathbf{t}$ and is shifted by angle δ.

Proof. The property is proved observing the expression of each transformed Gaussian kernel

$$\mathrm{n}\left(\mathbf{R}\ \mathbf{r} + \mathbf{t} - \boldsymbol{\mu}_i, \mathbf{\Sigma}_i\right) = \mathrm{n}\left(\mathbf{r} - \mathbf{R}^\top(\boldsymbol{\mu}_i - \mathbf{t}), \mathbf{R}^\top\mathbf{\Sigma}_i\mathbf{R}\right) \quad (20)$$

The transformed means $\boldsymbol{\mu}_i' = \mathbf{R}^\top(\boldsymbol{\mu}_i - \mathbf{t})$ and covariance matrices $\mathbf{\Sigma}_i' = \mathbf{R}^\top\mathbf{\Sigma}_i\mathbf{R}$ can be substituted in the ARS kernel terms in eq. (16) and (17) for each indices pair i, j. Vector $\mathbf{t}$ is canceled in the first term

$$a_{ij}'(\theta) = (\mathbf{u}_1^\top\mathbf{R}^\top(\boldsymbol{\mu}_i - \boldsymbol{\mu}_j))^2 = a_{ij}(\theta + \delta) \qquad (21)$$

whereas the second term is

$$b_{ij}'(\theta) = \mathbf{u}_1^\top\mathbf{R}^\top(\mathbf{\Sigma}_i + \mathbf{\Sigma}_j)\mathbf{R}\mathbf{u}_1 = b_{ij}(\theta + \delta) \qquad (22)$$

Thus, the translation on a GMM does not modify its ARS kernels and the rotation achieves a circular shift. $\square$

Such property allows decoupling of estimation of rotation and translation as explained in the next section.

IV. ESTIMATION OF ROTATION

The translation-invariance of ARS can be used to estimate the rotation between two planar GMMs representing the same scene observed from different viewpoints. Given $f_S(\mathbf{r})$ and $f_D(\mathbf{r})$ be respectively the density functions of the source and the destination point sets, the estimated rotation angle δ is the one which better overlaps the shifted spectrum of source set $\mathcal{S}\left[f_S\right](\theta + \delta^*)$ and the spectrum of destination set $\mathcal{S}\left[f_T\right](\theta)$. The proposed algorithm consists of the following steps:

1) simplification of the input source and destination GMMs $f_S(\mathbf{r})$ and $f_D(\mathbf{r})$;
2) computation of the Fourier coefficients of source and destination ARS;
3) computation of the Fourier coefficients of the correlation function;
4) estimation of maximum δ^* of correlation function.

This outlined algorithm is described in the following.

A. Simplification of Gaussian Mixture Models

The measurements provided by range sensors can be effectively modeled in the form of GMMs as previously discussed. The anisotropic ARS illustrated in section III can be applied to GMMs consisting of kernels with arbitrary covariance matrices. Such generalization offers theoretical and practical advantages. First, anisotropic ARS better fits the distribution of sensor uncertainty using the right covariance matrix. Second, an arbitrary input GMM can be approximated and substituted by another GMM with a lower number of Gaussian kernels. Thus, we propose a procedure for simplification and approximation of GMMs to significantly speed up the computation of ARS (quadratic in n_p).

Let $f^r(\mathbf{r})$ be the input GMM defined by parameters $\{(w_i^r, \boldsymbol{\mu}_i^r, \boldsymbol{\Sigma}_i^r)\}_{i=0,\dots,n_p^r}$ where w_i^r are the mixture weights, $\boldsymbol{\mu}_i^r$ the mean values and $\boldsymbol{\Sigma}_i^r$ the covariances. A significant application scenario occurs when the GMM consists of isotropic kernels, $\boldsymbol{\Sigma}_i^r = \sigma \mathbf{I}$. Simplification is achieved by substituting a subset of input Gaussians $\mathcal{I}_j$, called $f_{\mathcal{I}_j}^r(\mathbf{r})$, with the merged Gaussian $f_j^m(\mathbf{r})$, with parameters $(w_j^m, \boldsymbol{\mu}_j^m, \boldsymbol{\Sigma}_j^m)$, defined as

$$
\begin{aligned}
w_j^m &= \sum_{i \in \mathcal{I}_j} w_i^r \qquad \boldsymbol{\mu}_j^m = \frac{1}{w_j^m} \sum_{i \in \mathcal{I}_j} w_i^r \, \boldsymbol{\mu}_i^r \\
\boldsymbol{\Sigma}_j^m &= \sum_{i \in \mathcal{I}_j} \frac{w_i^r}{w_j^m} \left(\boldsymbol{\Sigma}_i^r + (\boldsymbol{\mu}_i^r - \boldsymbol{\mu}_j^m)(\boldsymbol{\mu}_i^r - \boldsymbol{\mu}_j^m)^\top \right)
\end{aligned}
\tag{23}
$$

Here, the superscript ^{r} denotes the reference input GMM whereas the superscript ^{m} refers to the merged GMM. The pre-conditions for merging are that the input kernels in $\mathcal{I}_j$ lie inside the same region of space, and that the difference between the merged Gaussian j and input kernel, measured according to a proper metric, is less then a given threshold.

The *normalized integral squared error* (NISE) [20] is taken as distance for comparing two distributions over their domain. The NISE between the distributions $f_{\mathcal{I}_j}(\mathbf{r})$ and $f_j^m(\mathbf{r})$ is defined as

$$
\text{nise}(f_j^m, f_{\mathcal{I}_j}^r) = \frac{D[f_{\mathcal{I}_j}^r - f_j^m]}{D[f_j^m] + D[f_{\mathcal{I}_j}^r]}
\tag{24}
$$

where the above integral norm $D[f]$ is defined as the integral of probability distribution f on the whole domain $\mathbb{R}^2$. In case $f_{\mathcal{I}_j}(\mathbf{r})$ is a sum of Gaussian kernels and $f_j^m(\mathbf{r})$ is a single Gaussian kernel, there are closed-form expressions for all the above terms:

$$
\begin{aligned}
D[f_{\mathcal{I}_j}^r - f_j^m] &= \sum_{i \in \mathcal{I}_j} w_j^m w_i^r \, \mathrm{n} \left(\boldsymbol{\mu}_i^r - \boldsymbol{\mu}_j^m, \boldsymbol{\Sigma}_i^r + \boldsymbol{\Sigma}_j^m \right) \\
D[f_{\mathcal{I}_j}^r] &= \sum_{i_1, i_2 \in \mathcal{I}_j} w_{i_1}^r w_{i_2}^r \, \mathrm{n} \left(\boldsymbol{\mu}_{i_1}^r - \boldsymbol{\mu}_{i_2}^r, \boldsymbol{\Sigma}_{i_1}^r + \boldsymbol{\Sigma}_{i_2}^r \right) \\
D[f_j^m] &= (w_j^m)^2 \, \mathrm{n} \left(0, \boldsymbol{\Sigma}_j^m \right)
\end{aligned}
\tag{25}
$$

The NISE measures the difference in probability concentration, has closed-form expression for GMMs and is bounded between 0 and 1. A subset $\mathcal{I}_j$ of Gaussian kernels from f^r, all locally concentrated in the same region, is merged into a single Gaussian kernel f^m when their NISE is less than the threshold $nise_{thr}$.

Algorithm 1 SimplifyGMM

1: **function** SIMPLIFYGMM($f^r := \{(w_i^r, \boldsymbol{\mu}_i^r, \boldsymbol{\Sigma}_i^r)\}_{i=0,\dots,n_p^r - 1}$)
2:     **Parameters**: $nise_{thr}$, q_{size}, q_{res}
3:     $levelmax \leftarrow \lceil \log_2(q_{size}/q_{res}) \rceil$;
4:     **for** $i = 0, \dots, n_p^r - 1$ **do**
5:         $\mathbf{k}_i^r \leftarrow \lfloor \boldsymbol{\mu}_i^r / q_{res} \rfloor$;
6:         $\mathcal{T}.insert(\{\mathbf{k}_i^r, w_i^r, \boldsymbol{\mu}_i^r, \boldsymbol{\Sigma}_i^r\})$;
7:     **end for**
8:     sort keys $\mathbf{k}_i^r$ in $\mathcal{T}$ in Morton order;
9:     $\mathcal{Q}.push([0, n_p^r[)$;
10:    $\mathcal{G} \leftarrow \emptyset$;
11:    **while** $\mathcal{Q} \neq \emptyset$ **do**
12:       $[l, u[\leftarrow \mathcal{Q}.pop()$;
13:       $h \leftarrow computeTreeLevel(l, u)$;   ▷ eq. (26)
14:       $\mathcal{I}_j \leftarrow \{i | l \leqslant i < u\}$;
15:       compute $f_j^m := (w_j^m, \boldsymbol{\mu}_j^m, \boldsymbol{\Sigma}_j^m)$ from $\mathcal{I}_j$; ▷ eq. (23)
16:       $nise_{cur} \leftarrow nise[f_j^m, f_{\mathcal{I}_j}^r]$;   ▷ eq. (24)
17:       **if** $h < levelmax$ and $nise_{cur} < nise_{thr}$ **then**
18:           $\mathcal{G} \leftarrow \mathcal{G} \cup \{(w_j^m, \boldsymbol{\mu}_j^m, \boldsymbol{\Sigma}_j^m)\}$;
19:       **else**
20:           $m \leftarrow splitInterval(\mathcal{T}, l, u)$;
21:           $\mathcal{Q}.push([l, m[)$;
22:           $\mathcal{Q}.push([m, u[)$;
23:       **end if**
24:    **end while return** simplified GMM $\mathcal{G}$;
25: **end function**

The procedure to simplify the reference input GMM is presented by Algorithm 1. The general idea is to merge a subset of Gaussian kernels belonging to the same region into a merged Gaussian, to check the accuracy of such substitution using NISE, and to split the region into smaller subregions when the error is above a threshold. The kernels lying in the same regions are detected using an implicit *quadtree*, which is implemented as a list $\mathcal{T}$ of GMM kernels sorted according to Morton order. Each mean vector $\boldsymbol{\mu}_i^r$ is encoded by its index vector $\mathbf{k}_i^r$ of the implicit grid of resolution q_{res} (line 5). List $\mathcal{T}$ is sorted in Morton order with respect to the keys $\boldsymbol{\mu}_i^r$ using Chan's *xor* trick [21].

In the main loop (lines 11-24), $\mathcal{T}$ is recursively split into smaller intervals until the simplified GMM is found. Each interval $[l, u[$ to be visited is extracted from queue $\mathcal{Q}$ and its level h in the quadtree (line 13) is computed as

$$
h = \max_{d=1,2} lev(k_{l,d}, k_{u,d}) \quad lev(a, b) = n_{bit} - nlz(a \oplus b) \tag{26}
$$

where n_{bit} is the number of bits of the integer type used for indices and $nlz()$ returns the number of leading zeros. Then, the algorithm assesses the Gaussian kernel f^m candidate for substituting the kernels $\mathcal{I}_j = [l, u[$ and evaluates the NISE (lines 15-16). If the NISE of the substitution is less than $nise_{thr}$ (and the tree level is large enough), f^m is added to output Gaussian kernel set $\mathcal{G}$. Otherwise, the interval $[l, u[$ is split on its largest span dimension (lines 20-22). Hereinafter we assume that ARSs are computed on simplified GMMs $\mathcal{G}$ and omit the superscripts ^{r} and ^{m}.

B. Fourier Expansion and Pairwise Correlation of ARS

The ARS in the form of Fourier series can be used to estimate the rotation between two GMMs representing the same scene observed from different viewpoints. Thanks to the

invariance of ARS to translation and its rotation-shift stated in proposition 1, the computation of rotation angle is decoupled from translation. We only need a convenient metric to measure the similarity of the ARS of two input GMMs.

Let $f_S(\mathbf{r})$ and $f_T(\mathbf{r})$ be respectively the density functions of the source and the target point sets, with $\mathcal{S}[f_S](\theta)$ and $\mathcal{S}[f_T](\theta)$ as their corresponding GMM-ARSs. Suppose that $f_T(\mathbf{r})$ represents the transformed version of $f_S(\mathbf{r})$, except for noise and field-of-view issues commonly occurring in perception problems. The rotation between $f_S(\mathbf{r})$ and $f_T(\mathbf{r})$ can be found by searching the angular shift δ that maximizes the overlap between the two spectra. The overlap is measured by

$$C[f_S, f_T](\delta) = \frac{1}{\pi} \int_0^\pi \mathcal{S}[f_S](\theta + \delta) \, \mathcal{S}[f_T](\theta) \, d\theta \quad (27)$$

that represents the correlation of the two spectra. The best alignment δ is found when the similarity $C[f_S, f_T](\delta)$ between the two spectra is maximum.

The computation of correlation in eq. (27) is complex and not convenient if the source and destination ARSs are in the form of eq. (18). Indeed, each ARS consists of $O(n_p^2)$ kernels, one for each pair of Gaussians, and a kernel-by-kernel comparison would be computationally expensive. A better approach is to express each ARS kernel $\varphi_{ij}(\theta)$ as the sum of orthogonal function bases. Since the functions $\varphi_{ij}(\theta)$ are π-periodic, the natural choice is its Fourier series. Thus, the Fourier series of the ARS $\mathcal{S}[f](\theta)$ of the GMM is obtained by summing the corresponding Fourier coefficients of each φ_{ij}.

The closed formula of Fourier coefficients for isotropic GMMs [13] cannot be trivially extended to the anisotropic case. Hence, the Fourier series of each point pair is computed using *Fast Fourier Transform* (FFT) on n_f samples $\varphi_{ij}(\theta_k)$ taken at equally spaced sampling points $\theta_k = k \, \pi/n_f$ for $k = 0, \ldots, n_f - 1$. Thus, the ARS of the GMMs in eq. (18) is approximated by the discrete Fourier

$$\mathcal{S}[f](\theta) \simeq a_0^f + \sum_{k=1}^{n_f} \left(a_k^f \cos(2k\theta) + b_k^f \sin(2k\theta) \right) \quad (28)$$

From the above expression of coefficients it is clear that the complexity of the estimation of $\{a_k^f, b_k^f\}_k$ is $O(n_p^2 \, n_f \log n_f)$. It is quadratic in the number of points n_p, since there is an ARS kernel for each pair of input Gaussian kernels. It is linearithmic with respect to the Fourier order n_f, since the coefficients are computed using FFT. In practice, a relative low order $n_f = 64$ is sufficient for accurate representation.

Then, the ARS $\mathcal{S}[f_S]$ and $\mathcal{S}[f_T]$ are expressed as Fourier series. We observe that the chosen correlation function $C[f_S, f_T]$ is a convolution of $\mathcal{S}[f_S]$ and $\mathcal{S}[f_T]$ and can also be represented as Fourier series. The formulas of the Fourier coefficients of $C[f_S, f_T]$, as well as the computation of its global maximum through a *branch-and-bound* (*B&B*) procedure, have been illustrated in our previous work [13]. The lower and upper bounds of correlation on any angular interval $[\underline{\theta}, \overline{\theta}]$ have been computed through simple interval arithmetic on sines and cosines of Fourier series. The splitting of a generic interval $[\underline{\theta}^*, \overline{\theta}^*]$ in *B&B* iterations stops when the
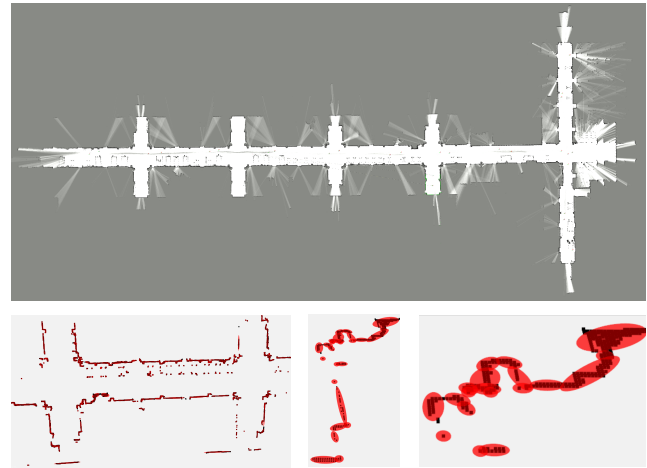

Fig. 2: Above: maps dataset sample from Cartographer output; Below: Gaussian simplification, zoomed at incremental levels of detail.

desired accuracy $\Delta\theta$ is reached, $\overline{\theta}^* - \underline{\theta}^* > \Delta\theta$. We can empirically observe that low-frequency coefficients of correlation are predominant and $C[f_S, f_T](\delta)$ is a rather smooth function, since it is obtained as a convolution. Thus, its global maxima are well defined.

C. Estimation of Translation

The goal of this paper is the estimation of rotation based on ARS. However, to illustrate the advantage of decoupling the estimation of translation and rotation, we also implemented a simple algorithm based on consensus to estimate the translation. Let $\{\bar{\boldsymbol{\mu}}_i^T\}_{i=1\ldots n_T}$ be the target point set and $\{\bar{\boldsymbol{\mu}}_j^S\}_{j=1\ldots n_S}$ be the mean values of source point set rotated according to the estimated rotation. Under the hypothesis that there is an overlap between the source and the destination point sets, there are pairs of corresponding Gaussian kernels i and j and their difference vector $\Delta\boldsymbol{\mu}_{ij} = \boldsymbol{\mu}_i^T - \bar{\boldsymbol{\mu}}_j^S$ is the translation vector up to correspondence inaccuracy and noise. Translation can be estimated by computing the histogram on a grid of all vectors $\Delta\boldsymbol{\mu}_{ij}$ for all pairs $i = 1 \ldots n_T$ and $j = 1 \ldots n_S$. The correctly associated pairs (i, j) belong to the same histogram bin, which should also correspond to the absolute maximum of the histogram. This approach is not computationally efficient and is affected by discretization, but it can provide a global estimation of translation once the rotation is given.

V. EXPERIMENTS

The experiments presented in this section are designed to assess the performance on rotation estimation of the proposed anisotropic ARS (ARS-Aniso) and to compare it with other state-of-the-art algorithms. The methods used in the experiments are the original isotropic ARS (ARS-Iso) [13], HS [11], PCA (Principal Component Analysis) [22], a standard implementation of ICP, VFC [2] and TEASER [4]. In the case of isotropic ARS, the input points are used as mean values of an isotropic GMM. In the case of anisotropic ARS, there is

TABLE I: Parameters configuration.

Description	Symbol	Value		
		mpeg7	maps	scans
ARS-Iso Fourier order	n_f		32	
ARS-Aniso Fourier order	n_f		64	
ARS standard deviation	σ_{min}	1.0	0.05	0.05
ARS tolerance on B&B	$\Delta\theta$		0.5°	
NISE threshold	$nise_{thr}$		0.15	
Quadtree resolution	q_{res}	1.0	0.05	0.05
Quadtree max quadrant size	q_{size}		$16 * q_{res}$	
HS angular resolution	$\Delta\theta_{hs}$	1.0	0.05	0.5
HS polar range resolution	$\Delta\rho_{hs}$	2.0	0.1	$0.05 \div 0.01$
HS polar range max	$\rho_{max,hs}$	400.0	400.0	150.0

more flexibility and the input GMM is simplified according to the procedure described in section IV-A. The implementations of ARS-Aniso, ARS-Iso and HS are available in public repository[1]. ICP, VFC and TEASER are local search methods and their performance depends on initial guess of rotation, which is given by PCA. Both VFC and TEASER are able to remove most wrong associations, but still rely on reasonable input estimation that is not guaranteed in our experiments. Moreover, TEASER is designed for 3D registration, not to deal with 2D point clouds. Three categories of datasets, discussed in the following subsections, have been used in the trials: the MPEG7 shape dataset, 3 occupancy map datasets, and 4 classic laser scan datasets. The parameters of the algorithms used in the experiments, in particular for isotropic and anisotropic ARS and HS, are reported in Table I. Some of the parameters have different values depending on the dataset scale. Precision and accuracy of methods across the different types of dataset are analyzed in the following subsections.

Table II reports the number of comparison trials (i.e. the number of pair map), the average execution times and the number of GMM kernels processed by ARS-Aniso, ARS-Iso and HS. The experiments have been performed on processor Intel Core i9-11900F@2.50GHz with 32GB RAM. The average execution times of ARS-Aniso for datasets *mpeg7*, *backpack2d*, *unipr-dia*, *fr079*, *intel-lab* and *mit-csail* is less than those of ARS-Iso. The reduced time is straightforwardly attributed to the reduction to about 10% of the number of GMM kernels achieved by the procedure described in section IV-A. When such reduction is not achieved (*backpack3d*) or is limited (*fr-clinic*), the flexibility of ARS-Aniso cannot be exploited. HS generally outperforms (sometimes only slightly) both ARS methods in terms of speed, but it requires parameter tuning and suffers from relative speed as discussed in section V-C.

A. MPEG7 Dataset

The original MPEG-7 database [23] consists of 1440 images of different shapes representing objects or animals. The contour points are used as noisy input points. The point set is translated and rotated according to known parameters and then distorted to assess the robustness in rotation estimation. The rotation angles are uniformly distributed on interval $[0, 180]$ deg, whereas the translation is uniformly distributed up to a maximum value approximately corresponding to the
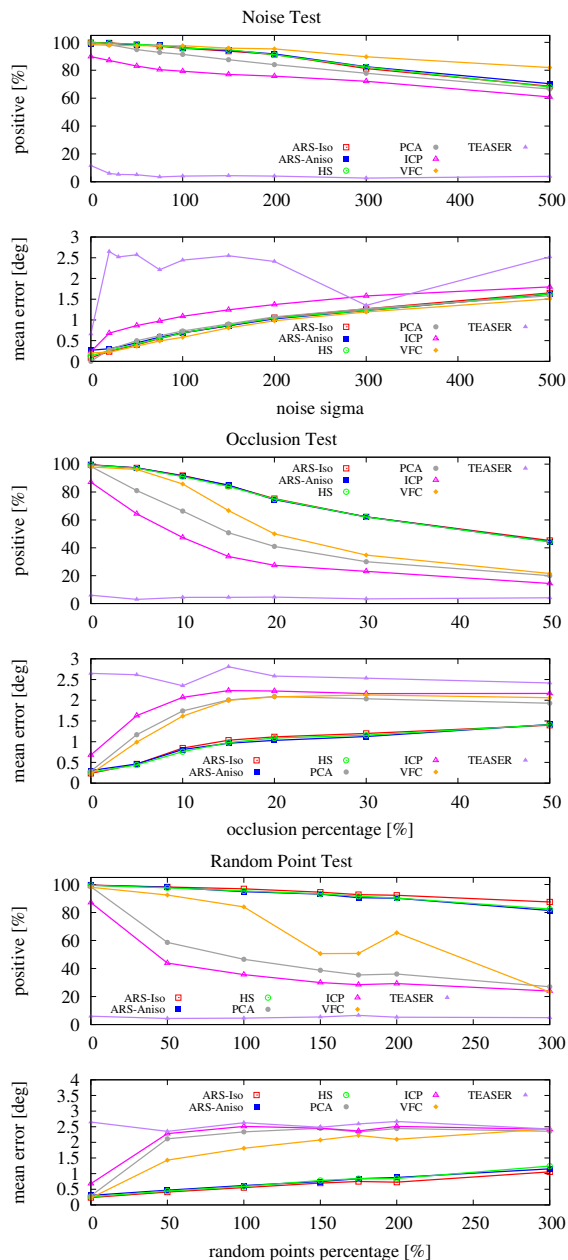
[1]https://github.com/dlr1516/ars

Fig. 3: Positive estimation percentage (top) and mean angular error (bottom) obtained by ARS-Aniso, ARS-Iso, HS, PCA, ICP, VFC and TEASER on three experiments: (a) additive Gaussian *noise* with different standard deviation σ_{noise}, (b) *occlusion* with different occlusion rates β (in percentage), (c) *random points* with different rates γ (in percentage).

dimension of the object. Since this dataset has been used in our previous work [13], we briefly recapitulate the three kinds of distortion applied to the original point sets.

1) *Noise*. A Gaussian noise with standard deviation σ_{noise} in interval $0 \div 50$ is applied to each point coordinate.
2) *Occlusion*. All the points inside a circle centered in a randomly selected point of the set and with radius equal to a portion β of the dimension of the shape are removed ($\beta \in 0 \div 50\%$).
3) *Random Points*. The input set of n_{in} points is augmented

TABLE II: Execution Time Results

dataset	type	trial num	avg points num	avg kernel num	ARS-Aniso GMM kernel ratio	avg time [ms]	ARS-Iso avg time [ms]	HS avg time [ms]
mpeg7	images	1400	1444	30.93	8.99 %	129.81	376.29	2.08
backpack2d	maps	419	2140	177.19	8.28 %	13.30	625.02	5.82
backpack3d	maps	134	968	967.62	100.00 %	424.17	146.83	4.19
unipr-dia	maps	25	4100	340.74	8.31 %	54.49	2473.42	8.84
fr079	scans	1023	360	53.13	14.76 %	2.32	14.25	1.80 ÷ 14.13
fr-clinic	scans	377	180	136.43	75.69 %	13.93	3.51	1.63 ÷ 13.67
intel-lab	scans	905	180	39.61	22.01 %	1.47	3.66	1.46 ÷ 13.86
mit-csail	scans	760	361	53.53	14.83 %	2.60	14.23	1.81 ÷ 13.97

by γn_{in} random points ($\gamma \in 0 \div 300\%$) drawn from a uniform distribution over the shape.

Figures 3(a)-(c) illustrate the results achieved using the discussed algorithms. The mean angular error is computed only on positives, i.e. with error less than $5°$. Effective local registration algorithms like VFC perform well only on the noise distortion experiments, where the contour outline is preserved and point-to-point association is feasible. The poor performance of state-of-the-art TEASER may be attributed to inaccuracy of correspondences, to ineffectual tuning of parameters and to issues related to the application of a 3D registration algorithm to 2D domain. Most trials of TEASER terminate with the validity flag unset due to inconsistency in graph-based inference. More investigation is required to understand the problem. In all other cases, the global correspondence-less methods ARS-Aniso, ARS-Iso and HS outperform the other techniques. In particular, they have similar results in occlusion tests since they are based on collinearity of points. The error of ARS-Aniso is usually close and intermediate between those achieved by ARS-Iso and HS.

B. Occupancy Grid Map Datasets

The second group of tests has been performed on GMMs generated from occupancy grid maps. The three datasets are *backpack2d* and *backpack3d* from the collection of Deutsches Museum, and *unipr-dia* acquired in the main hallways of the Dipartimento di Ingegneria e Architettura of the University of Parma. The raw laser scans and odometry measurements from these datasets have been processed by mapping tool *Carthographer* [24]. The maps built by Carthographer consist of several local occupancy grid submaps, which are used for rotation estimation. The cell centers of each occupancy grid submap are used as the mean values of an associated GMM.

The rotation estimation experiments are performed as follows. We select the candidate pairs of maps to be compared based on their index in the general map, which the Carthographer generally assigns according to the trajectory traveled by the robot. The majority of the maps with consecutive index are partially overlapping. The Carthographer tends to initialize the submap reference frames with orientation close to the origin frame. Thus, we manually added a random rotation to all the maps for testing arbitrary orientations.

The performances on rotation estimation of the compared algorithms are summarized in Figure 4. The first histogram represents the number of negative trials, i.e. with estimation error

greater than $3°$. Several negatives are due to non-overlapping submaps, even though with consecutive indices. The average rotation errors of ARS-Aniso, ARS-Iso and HS are close to $0.2°$ and are significantly lower than those achieved by local methods. ARS-Aniso performance is comparable to ARS-Iso and HS with no clear predominance of one method over the others.

C. Laser Scan Datasets

The third group of tests has been conducted on standard benchmarks of laser scans for robot localization and mapping applications: *fr079*, *fr-clinic*, *intel-lab* and *mit-csail*. Each of said datasets contains about 5000 scans. The goal of the experiments that have been run is to correctly estimate the rotation between subsequent scans in each dataset, and comparing the results obtained with the already mentioned six methods through the ground truth information contained in the datasets. Results are reported in figure 5. Only subsequent scans with reciprocal ground truth rotations of at least $3°$ have been considered in order not to overrate the algorithm performance when limited rotation occurs. As for the Occupancy Grid Map experiments, several negative estimations are due to non-overlapping scans. The better results are achieved by ARS-Iso, ARS-Aniso and HS. For the latter dataset, an additional set of tests has been performed, in order to further assess the comparison between the mean execution times of ARS-Aniso and HS. By varying the HS polar range resolution from 0.05 to 0.01 (see corresponding line in table I), the mean execution time of HS, initially lower the ones of both ARSs, saw a noticeable increase of up to 10 times.

VI. CONCLUSION

This work has presented the anisotropic Angular Radon Spectrum, a novel method for global estimation of rotation in two dimension spaces. The algorithm extends the isotropic spectrum and operates on GMMs with arbitrary kernel covariances. We have derived the general analytical expression of RT of GMMs and of the corresponding ARS. Moreover, we have proposed a procedure for simplifying the GMMs based on implicit quadtrees and NISE, the numerical computation of Fourier coefficients of anisotropic ARS, and the estimation of the rotation angle as the maximum of correlation function. The proposed method has been implemented and compared with other state-of-the-art algorithms. Experiments have been executed on datasets from shape images, occupancy grid
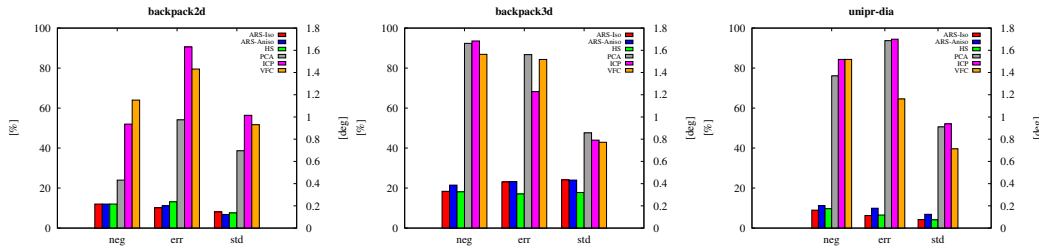
Fig. 4: Negative estimation percentage, average rotation mean error [°] and standard deviation obtained in rotation accuracy tests on occupancy grid datasets *backpack2d*, *backpack3d* and *unipr-dia* (from left to right).
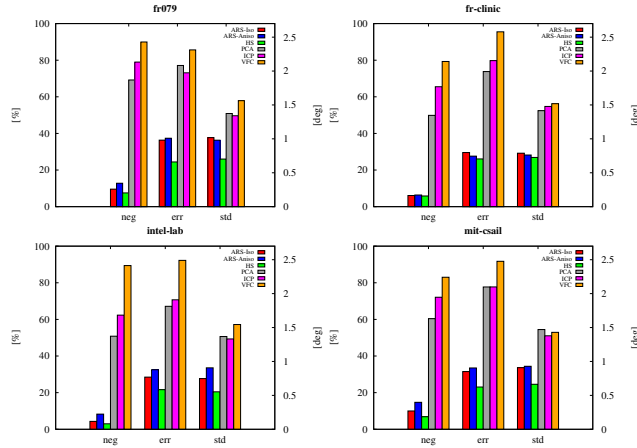

Fig. 5: Negative estimation percentage, average rotation mean error [°] and standard deviation obtained in rotation accuracy tests on scan datasets *fr079*, *fr-clinic*, *intel-lab* and *mit-csail* (from left to right, top to bottom).

maps and laser scans. The proposed anisotropic ARS achieves performance comparable to other global methods, but it allows larger adaptation to arbitrary GMMs and potential reduction in execution time. In future works, we expect to extend Angular Radon Spectrum to the estimation of rotation in space and to exploit its potential in a complete mapping pipeline. The 3D ARS will capture the point cloud coplanarity and its computational complexity is expected to be also quadratic in the number of GMM kernels.

REFERENCES

[1] M. Magnusson, A. Lilienthal, and T. Duckett, "Scan registration for autonomous mining vehicles using 3d-ndt," *Journal of Field Robotics*, vol. 24, no. 10, pp. 803–827, 2007.

[2] J. Ma, J. Zhao, J. Tian, A. Yuille, and Z. Tu, "Robust Point Matching via Vector Field Consensus," *IEEE Transactions on Image Processing*, vol. 23, no. 4, pp. 1706–1721, April 2014.

[3] D. Holz, A. Ichim, F. Tombari, R. Rusu, and S. Behnke, "Registration with the point cloud library: A modular framework for aligning in 3-d," *IEEE Robotics Automation Magazine*, vol. 22, no. 4, pp. 110–124, Dec 2015.

[4] H. Yang, J. Shi, and L. Carlone, "Teaser: Fast and certifiable point cloud registration," *IEEE Transactions on Robotics*, vol. 37, no. 2, pp. 314–333, 2020.

[5] F. Bai and A. Bartoli, "Procrustes analysis with deformations: A closed-form solution by eigenvalue decomposition," *Int. J. Comput. Vis. (IJCV)*, vol. 130, pp. 567–593, 2022.

[6] J. Yang, H. Li, D. Campbell, and Y. Jia, "Go-ICP: A Globally Optimal Solution to 3D ICP Point-Set Registration," *IEEE Trans. on Pattern Analysis and Machine Intelligence*, vol. 38, no. 11, pp. 2241–2254, Nov 2016.

[7] L. Consolini, M. Laurini, M. Locatelli, and D. Lodi Rizzini, "A second-order lower bound for globally optimal 2d registration," *CoRR*, vol. abs/1901.09641, 2020. [Online]. Available: http://arxiv.org/abs/1901.09641

[8] J. Straub, T. Campbell, J. How, and J. Fisher, "Efficient global point cloud alignment using bayesian nonparametric mixtures," in *Proc. IEEE Conference on Computer Vision and Pattern Recognition (CVPR)*, 2017, pp. 2941–2950.

[9] W. Clark, M. Ghaffari, and A. Bloch, "Nonparametric continuous sensor registration," *Journal of Machine Learning Research*, vol. 22, no. 271, pp. 1–50, 2021. [Online]. Available: http://jmlr.org/papers/v22/20-1468.html

[10] R. Zhang, T.-Y. Lin, C. Lin, S. Parkison, W. Clark, J. Grizzle, R. Eustice, and M. Ghaffari, "A new framework for registration of semantic point clouds from stereo and rgb-d cameras," in *Proc. of the IEEE Int. Conf. on Robotics & Automation (ICRA)*, 2021, pp. 12 214–12 221.

[11] A. Censi, L. Iocchi, and G. Grisetti, "Scan Matching in the Hough Domain," in *Proc. of the IEEE Int. Conf. on Robotics & Automation (ICRA)*, 2005.

[12] A. Censi and S. Carpin, "HSM3D: feature-less global 6DOF scan-matching in the Hough/Radon domain," in *Proc. of the IEEE Int. Conf. on Robotics & Automation (ICRA)*, 2009, pp. 3899–3906.

[13] D. Lodi Rizzini, "Angular Radon Spectrum for Rotation Estimation," *Pattern Recognition*, vol. 84, pp. 182–196, dec 2018.

[14] A. Makadia and K. Daniilidis, "Rotation recovery from spherical images without correspondences," *IEEE Trans. on Pattern Analysis and Machine Intelligence*, vol. 28, no. 7, pp. 1170–1175, 2006.

[15] L. Bernreiter, L. Ott, J. Nieto, R. Siegwart, and C. Cadena, "Phaser: A robust and correspondence-free global pointcloud registration," *IEEE Robotics and Automation Letters*, vol. 6, no. 2, pp. 855–862, 2021.

[16] E. Olson, "Real-time correlative scan matching," in *Proc. of the IEEE Int. Conf. on Robotics & Automation (ICRA)*, 2009, pp. 4387–4393.

[17] S. Deans, "Radon and Abel Transforms," in *The Transforms and Applications Handbook*, 2nd ed., A. Poularikas, Ed.   CRC Press, 2000, pp. 1–95.

[18] A. Papoulis, *Probability, Random Variables, and Stochastic Processes*, 3rd ed.   McGraw Hill, 1991.

[19] K. Petersen and M. Pedersen, "The Matrix Cookbook," Nov 2012, version 20121115. [Online]. Available: http://www2.imm.dtu.dk/pubdb/p.php?3274

[20] D. Crouse, P. Willett, K. Pattipati, and L. Svensson, "A look at gaussian mixture reduction algorithms," in *14th International Conference on Information Fusion*, 2011, pp. 1–8.

[21] M. Connor and P. Kumar, "Fast construction of k-nearest neighbor graphs for point clouds," *IEEE Trans on Visualization and Computer Graphics*, vol. 16, no. 4, pp. 599–608, 2010.

[22] R. Hoover, A. Maciejewski, and R. Roberts, "Eigendecomposition of images correlated on, and using spectral theory," *Image Processing, IEEE Transactions on*, vol. 18, no. 11, pp. 2562–2571, 2009.

[23] X. Bai, X. Yang, L. Latecki, W. Liu, and Z. Tu, "Learning context-sensitive shape similarity by graph transduction," *IEEE Trans. on Pattern Analysis and Machine Intelligence*, vol. 32, no. 5, pp. 861–874, May 2010.

[24] W. Hess, D. Kohler, H. Rapp, and D. Andor, "Real-Time Loop Closure in 2D LIDAR SLAM," in *Proc. of the IEEE Int. Conf. on Robotics & Automation (ICRA)*, 2016, pp. 1271–1278.